ELSEVIER

Volume 204 August 2013 ISSN 0022-4596

JOURNAL OF SOLID STATE CHEMISTRY

IN THIS ISSUE:

Structural characterization and low-temperature physical properties of p-type single-crystal $K_8Ga_{8.5}Sn_{37.5}$ grown by self-flux method

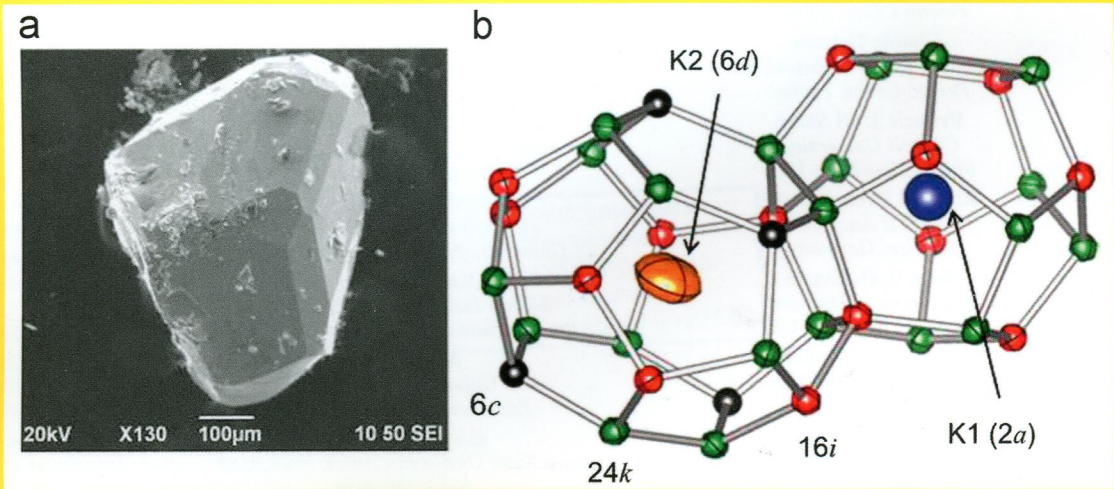

Stevce Stefanoski, Yongkwan Dong and George S. Nolas

Available online at www.sciencedirect.com

SciVerse ScienceDirect

ELSEVIER

Volume 204, August 2013

JOURNAL OF SOLID STATE CHEMISTRY

www.elsevier.com/locate/jssc

CONTENTS

Abstracted/indexed in BioEngineering Abstracts, Chemical Abstracts, Coal Abstracts, Current Contents/Physics, Chemical, & Earth Sciences, Engineering Index, Research Alert, SCISEARCH, Science Abstracts, and Science Citation Index. Also covered in the abstract and citation database SciVerse SCOPUS®. Full text available on SciVerse ScienceDirect®.

Regular Articles

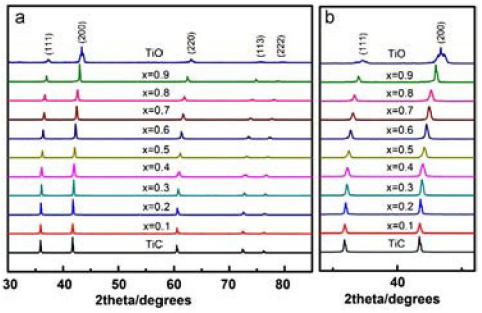

XRD of series of titanium oxycarbides ($TiC_{1-x}O_x$, $0 \le x \le 1$) solid solution prepared by adjusting the proportion of TiO in the starting material.

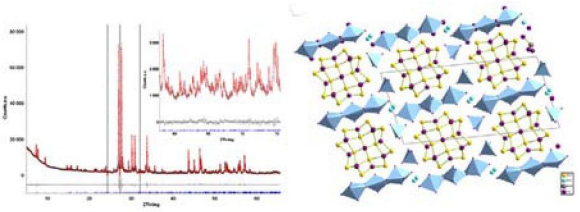

Measured and calculated diffraction spectra for $Bi_{12.8}Co_{0.2}Mo_5O_{34\pm\delta}$ and projection of the $Bi_{12.8}Co_{0.2}Mo_5O_{34\pm\delta}$ crystal structure onto the *ac* plane.

Regular Articles—Continued

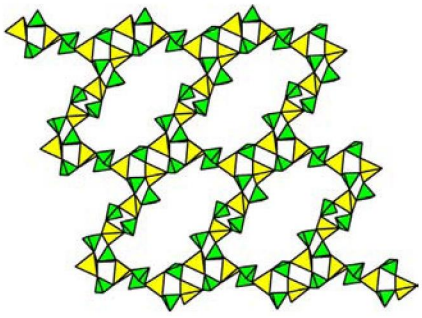

The first layered metal phosphite with large 20-ring windows, (C8H17NH3)4Zn3(HPO3)5 · 3H2O (1), sandwiched by water molecules and protonated *tert*-octylamine molecules.

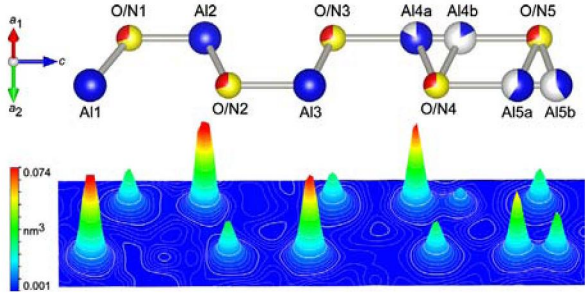

A bird's eye view of electron densities up to 50% (0.074 nm^{-3}) of the maximum on the plane parallel to (110) with the corresponding atomic arrangements of $Al_9O_3N_7$.

Continued

Growth of single crystalline TaON on yttria-stabilized zirconia (YSZ)
Junguang Tao, J.W. Chai, L.M. Wong, Z. Zhang, J.S. Pan and S.J. Wang
page 27

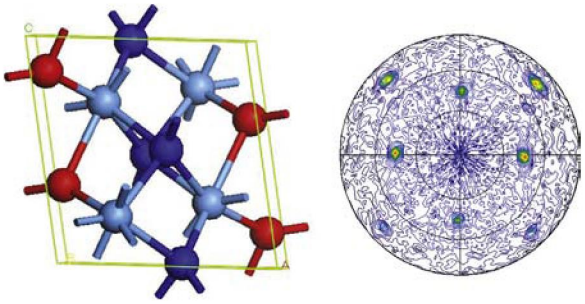

Structure of single crystalline β-TaON and its diffraction pole figure.

Crystals, magnetic and electronic properties of a new $ThCr_2Si_2$-type $BaMn_2Bi_2$ and K-doped compositions
Bayrammurad Saparov and Athena S. Sefat
page 32

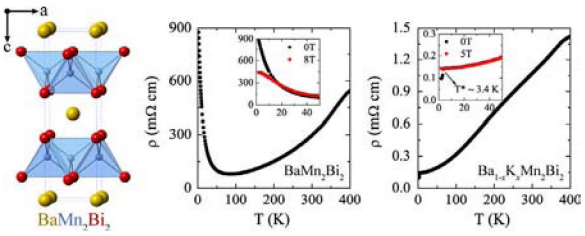

Local moment antiferromagnet $BaMn_2Bi_2$, the first bismuthide with $ThCr_2Si_2$ structure, turns metallic upon K-doping.

Crystal structure and magnetic properties and Zn substitution effects on the spin-chain compound $Sr_3Co_2O_6$
Xia Wang, Yanfeng Guo, Ying Sun, Yoshihiro Tsujimoto, Yoshitaka Matsushita and Kazunari Yamaura
page 40

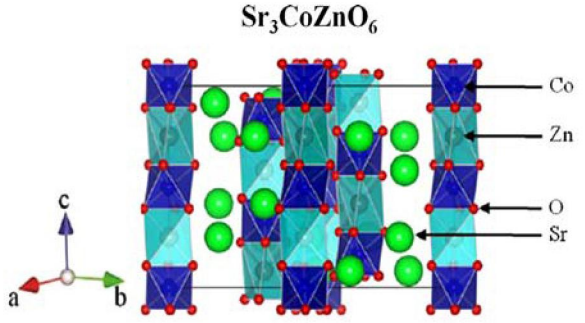

Crystal structure of the spin-chain compound Sr_3CoZnO_6 synthesized at 6 GPa. Zn atoms preferably occupy the trigonal prism sites rather than the octahedral sites. As a result, the compound is much magnetically isotropic.

High-pressure synthesis and characterization of the first cerium fluoride borate CeB_2O_4F
Ernst Hinteregger, Klaus Wurst, Martina Tribus and Hubert Huppertz
page 47

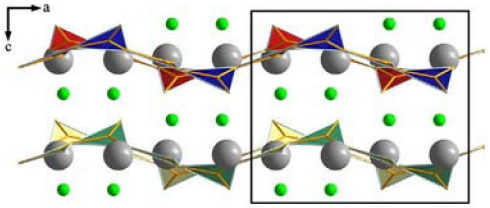

A new rare-earth fluoride borate CeB_2O_4F could be synthesized under high-pressure/high-temperature conditions of 0.9 °GPa and 1450 °Cin a Walker-type multianvil apparatus. The crystal structure represents a new structure type in the class of rare-earth fluoride borates. The structure exhibits a 9 + 1 coordinated cerium ion, one three-fold coordinated fluoride ion and a one-dimensional chain of $[BO_3]^{3-}$ groups. A closer view on the *ac*-plane shows an interesting wave-like modulation of the borate chains.

A microporous metal–organic framework with butynelene functionality for selective gas sorption
Lifeng Wang, Lu Zhai, Xiaoming Ren and Wenwei Zhang
page 53

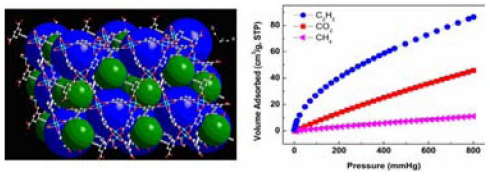

A microporous metal–organic framework with butynelene groups, $\{[Cu_2(BBTC)(H_2O)_2]\cdot 2DMSO\cdot 4H_2O\}_n$, exhibits higher gas selective sorption towards C_2H_2/CH_4 and CO_2/CH_4 at room temperature with a selectivity of 5.7 and 4.1, respectively.

$K[AsW_2O_9]$, the first member of the arsenate–tungsten bronze family: Synthesis, structure, spectroscopic and nonlinear optical properties
Evgeny V. Alekseev, Olivier Felbinger, Shijun Wu, Thomas Malcherek, Wulf Depmeier, Giuseppe Modolo, Thorsten M. Gesing, Sergey V. Krivovichev, Evgeny V. Suleimanov, Tatiana A. Gavrilova, Lev D. Pokrovsky, Alexey M. Pugachev, Nikolay V. Surovtsev and Victor V. Atuchin
page 59

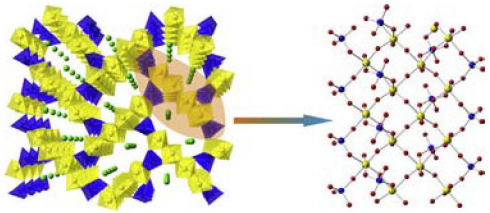

$K[AsW_2O_9]$, the first member of arsenate–tungsten bronze family exhibit new three dimensional structure type, significant thermal stability and NLO properties.

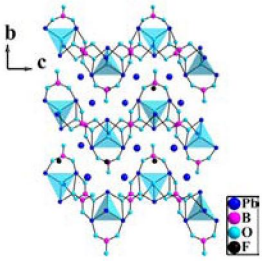

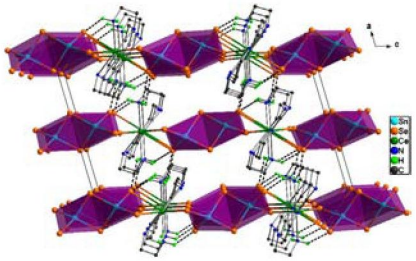

New lanthanide complexes concerning the Sn_2Se_6 ligand were solvothermally prepared, and the effect of ethylene polyamines on the complexation of Sn_2Se_6 with Ln(III) centers are observed.

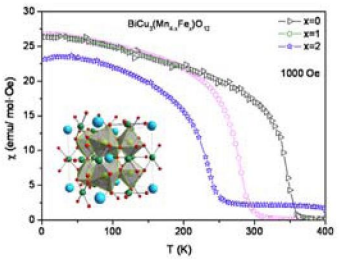

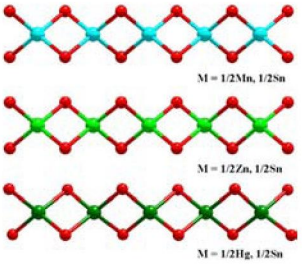

Three new one-dimensional ternary selenidostannates, [DBNH][$M_{1/2}Sn_{1/2}Se_2$] (M = Mn (1), Zn (2), Hg (3); DBN = 1,5-diazabicyclo[4.3.0]non-5-ene), have been synthesized under solvothermal condition.

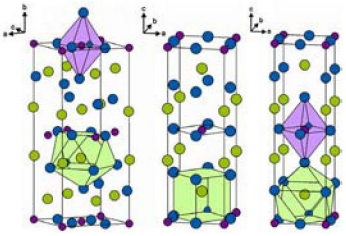

Crystal structure of T^x (orthorhombic), T' and T (tetragonal) modifications of La_2CuO_4 (left to right). The space group for orthorhombic T^x is *Cmce* and *I4/mmm* for both T' and T structures; copper cations are presented as small purple, lanthanum as large blue and oxygen as large green circles.

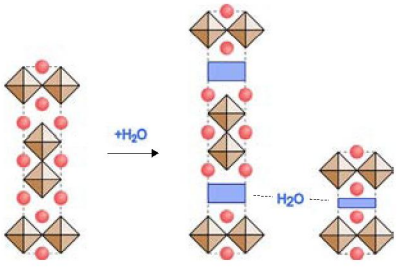

Many of the Ruddlesden–Popper-structured $A_3B_2O_{7-\delta}$ oxides readily react with water via intercalation reactions. Three possible factors affecting the water intercalation are identified: oxygen content of the phase, ionic radius of cation A and valence state of cation B. The resultant layered water-derivative phases can be categorised into two groups, depending on the crystal symmetry of the phase.

Continued

Complex long-range magnetic ordering in the Mn-bearing dugganite $Pb_3TeMn_3P_2O_{14}$

H.J. Silverstein, A.Z. Sharma, K. Cruz-Kan, H.D. Zhou, A. Huq, R. Flacau and C.R. Wiebe

page 102

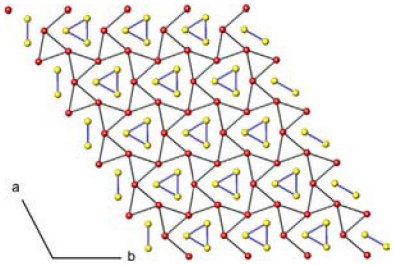

Two geometrically frustrated cationic substructures of the langasites and dugganites have profound effects on the magnetism of these compounds. In $Pb_3TeMn_3P_2O_{14}$, Mn^{2+} ($S = 5/2$) isolated trinuclear units are shown in yellow, while the red distorted kagomé network is nonmagnetic. (For interpretation of the references to color the reader is referred to the web version of this article.)

A $p \rightarrow n$ transition for Sn-doped Cu(In,Ga)Se_2 bulk materials

Mehrdad Monsefi and Dong-Hau Kuo

page 108

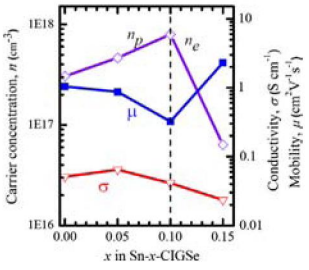

The controls in defect type and electrical properties of Cu(In,Ga)Se_2 by doping Sn^{4+} on the In^{3+} site.

Synthesis, crystal structure and properties of $Mg_3B_{36}Si_9C$ and related rare earth compounds $RE_{3-x}B_{36}Si_9C$ (RE = Y, Gd–Lu)

Thilo Ludwig, Alexis Pediaditakis, Vanessa Sagawe and Harald Hillebrecht

page 113

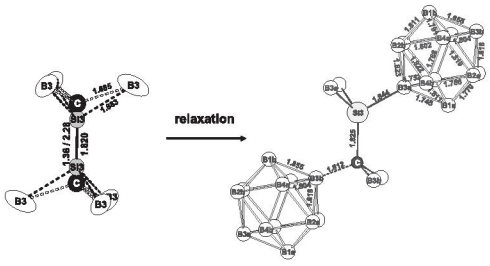

Single crystals of the new boridesilicide $Mg_3B_{36}Si_9C$ were obtained from the elements in a Si-melt. Besides B_{12}-icosahedra and ethan-like Si_8-units it contains a disordered SiC-dumbbell. Correct distances were obtained by relaxation calculation based on the X-ray data.

The study of magnetic phase diagram of $Fe_{1-x}Zn_xCr_2S_4$ solid solutions

T.G. Aminov, D.I. Kirdyankin, G.G. Shabunina and V.M. Novotortsev

page 123

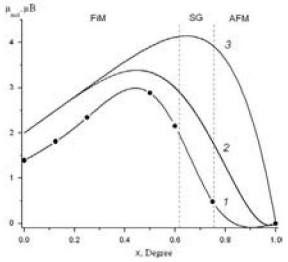

Saturation magnetic moment of the solid solutions $Fe_{1-x}Zn_xCr_2S_4$ at $T = 5$ K: 1—experimental curve; 2—theoretical curve on [15]; 3—theoretical curve on [16].

Intermolecular interactions between imidazole derivatives intercalated in layered solids. Substituent group effect

M. González, A.A. Lemus-Santana, J. Rodríguez-Hernández, C.I. Aguirre-Velez, M. Knobel and E. Reguera *page 128*

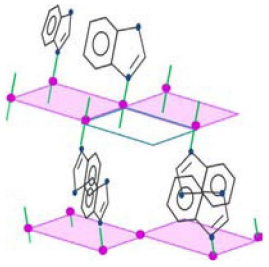

In the interlayers region imidazole derivative molecules are oriented according to their dipolar and quadrupolar interactions and minimizing the steric impediment.

Defect disorder in UO_2

A.-R. Hassan, Anter El-Azab, Clarissa Yablinsky and T. Allen

page 136

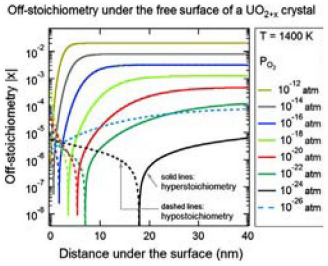

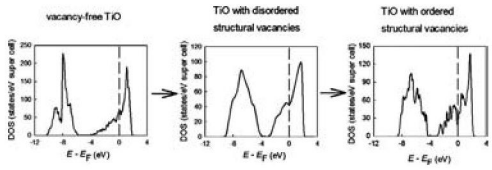

Changes in total DOS of titanium monoxide when going from vacancy-free TiO to TiO with disordered structural vacancies and to TiO with ordered structural vacancies.

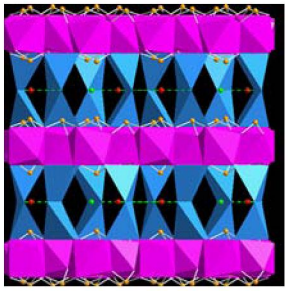

A metal selenite halide has been synthesized and features a 3-D open-framework structure, composing edge-shared CdO_8 decahedra and pillars of edge-sharing pentahedra. UV–vis, TG–DSC and luminescent measurements are also reported.

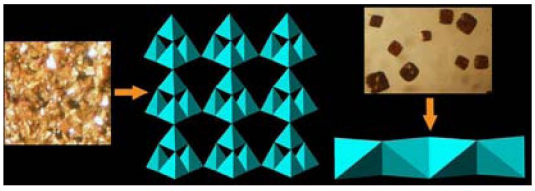

Two polymorphic forms of $[NH_4][InSe_2]$, which are yellow and red, have been prepared and their optical properties investigated.

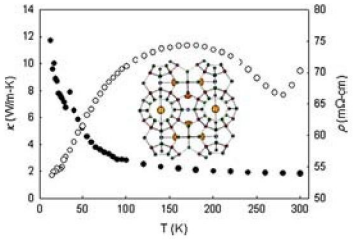

Single-crystal $K_8Ga_{8.5}Sn_{37.5}$ was synthesized via a double-flux method where Ga and Sn were used as fluxes. Large disorder for K inside the larger polyhedra in the crystal structure of $K_8Ga_{8.5}Sn_{37.5}$ was observed. Measurements of the electronic properties indicate p-type conduction with the onset of minority charge carrier conduction at temperatures above 270 K.

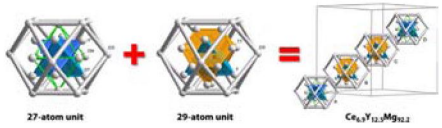

Reported is the Mg-rich intermetallic compounds $Y_{5-x}Mg_{24+x}$ series adopting the cubic α-Mn type structure and its complex ternary derivative $Ce_{6.9}Y_{12.5}Mg_{92.2}$ crystallized in a defect $Sm_{11}Cd_{45}$ type structure with a nearly twice larger lattice parameter than those of the $Y_{5-x}Mg_{24+x}$ series. Electronic structure calculations show nearly free electron like behavior, but with a distinctive pseudogap in the density of states curve for the ternary system.

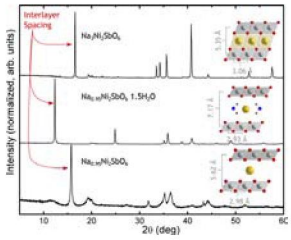

Powder diffraction patterns of $Na_3Ni_2SbO_6$, $Na_{0.95}Ni_2SbO_6\cdot 1.5H_2O$ and $Na_{0.95}Ni_2SbO_6$. Each pattern has been normalized in intensity. Cartoons depict the change in layer separation with hydration and give the approximate distances between layers and Ni atoms.

Continued

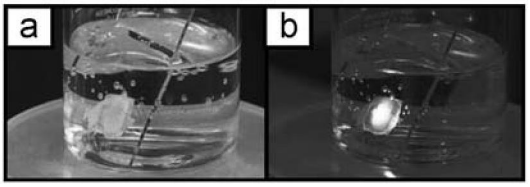

Obtained 8-coordinated SrO:Eu^{2+} phosphor exhibit strong blue luminescence in distilled water.

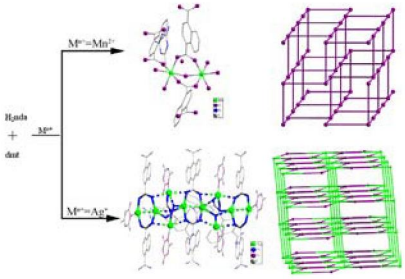

Two new transition metal coordination complexes **1**–**2** have been hydrothermally synthesized and characterized by single-crystal X-ray diffraction, IR spectra, elemental analysis thermogravimetric analysis (TGA).

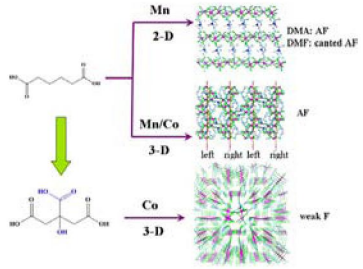

Five new Mn(II)/Co(II) coordination polymers display 2-D/3-D structures containing 1-D carboxylate–metal chains or wheel clusters. Magnetic analyses reveal that they show antiferromagnetic, canted antiferromagnetic and weak ferromagnetic behaviors, respectively.

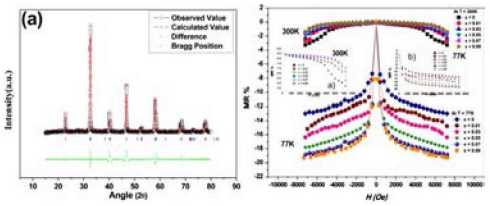

The magnetic, electrical and magnetoresistance behavior of Nickel doped $La_{2/3}Sr_{1/3}Mn_{1-x}Ni_xO_3$ ($0.00 \le x \le 0.09$) samples have been studied systematically.

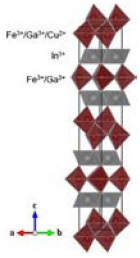

Solid solution of $In_2Fe_{2-x}Ga_xCuO_7$ has been synthesized and analyzed with powder X-ray diffraction and DC magnetic susceptibility studies. The magnetic ground state has been investigated through cation substitution and compared to that of $InFe_{1-x}Ga_xCuO_4$.

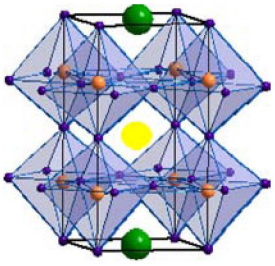

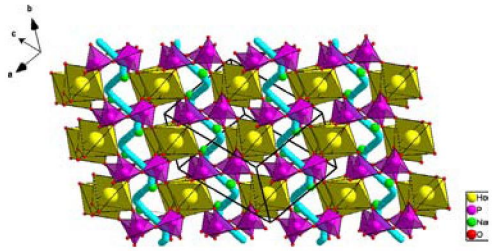

Schematic representation of the structural arrangement of $NaHoP_2O_7$ shows the sodium conduction pathway along the [0 1 0] direction.

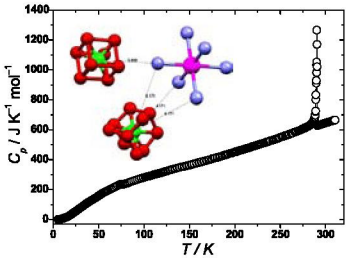

Molar heat capacities obtained for $[Ru(NH_3)_6](ClO_4)_3$ at temperatures between 5 and 310 K. Molecular structure of $[Ru(NH_3)_6]^{3+}$ and two types of ClO_4^- varying in dynamic disorder at 293 K.

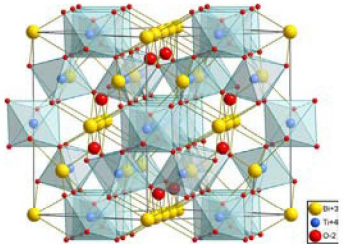

The ideal crystal structure of pyrochlore $A_2B_2O_6O'$ (A—Bi^{3+}, Fe^{3+}; B—Ti^{4+}, Fe^{3+}).

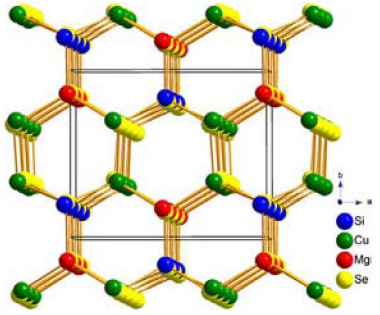

Three new diamond-like compounds, Cu_2MgSiS_4, Cu_2MgGeS_4, and $Cu_2MgSiSe_4$, have been synthesized. All the three compounds crystallize in the space group $Pmn2_1$ and all atoms are tetrahedrally coordinated.

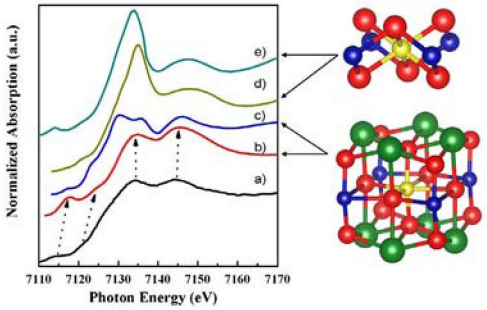

The Fe *K*-edge XANES spectra of: (a) experimental result in comparison to the simulated spectra when Fe atoms were substituted in the RS layer; (b) with magnetic moment; (c) without magnetic moment, and in the CoO_2 layer; (d) with magnetic moment and (e) without magnetic moment.

Continued

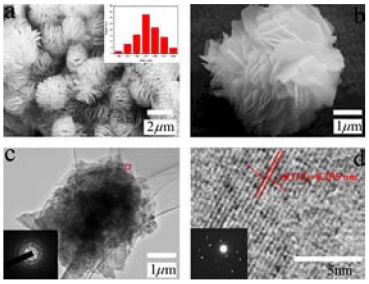

Low and high-magnification SEM images demonstrate the perfect flower-like $NaY(MoO_4)_2$ prepared in the presence of PVP; Detailed TEM and HRTEM images further manifest the single-crystalline feature.

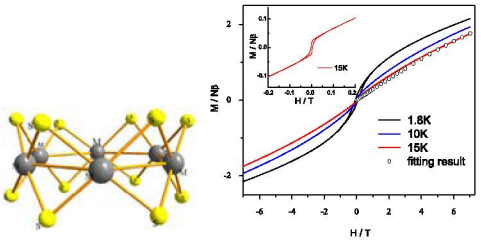

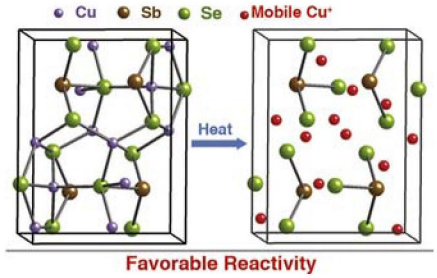

Cu_3SbSe_3 mobile phase is likely the key species to promote the formation of $Cu(In,Ga)Se_2$, and significantly promoting effect by Sb is also found in the synthesis of $Cu(In,Ga)Se_2$ nanocrystals.

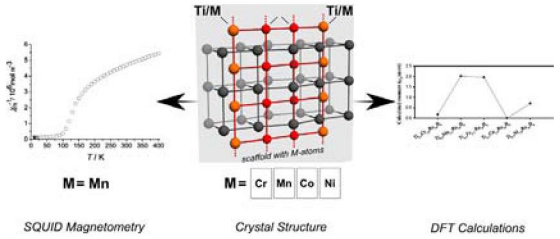

The crystal structures of the new phases (M = Cr, Mn, Co, Ni) are confirmed by Rietveld refinement of powder diffraction data and single crystal X-ray diffraction (for M = Co) to contain beside the M-ladder also M/Ti-chains. Similar to the series $Ti_9M_2Ru_{18}B_8$, the crystal structure of the new phases are mainly stabilized by the heteroatomic Ru–B and Ru–Ti bonds that remain nearly constant throughout the series, whereas the M-containing bonds vary significantly with varying valence electron count. An experimental finding confirmed and even extended by COHP bonding analyses. In addition, the DOS analyses of the M-elements reveal the development of magnetic moments for the M = Mn, Ni cases but not for M = Co. Indeed, $Ti_8Co_3Ru_{18}B_8$ was found experimentally to be a paramagnet and ferrimagnetic ordering below 120 K is found for M = Mn.

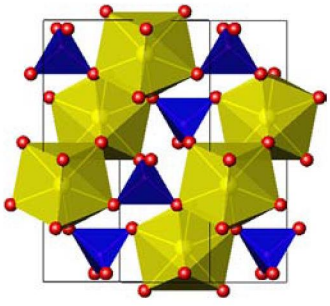

Large fergusonite-type $CeNbO_4$ crystals were prepared for the first time in a floating zone mirror furnace. Crystal growth in an argon atmosphere yielded a single phase monoclinic $CeNbO_4$, as confirmed by selected area electron diffraction, powder and single crystal X-ray diffraction. The structure was determined in the standard space group setting C12/c1 (No. 15), rather than the commonly adopted I12/a1. AC impedance spectroscopy found $CeNbO_4$ single crystals showed lower conductivity compared to $CeNbO_{4+\delta}$ confirming interstitial oxygen can penetrate through fergusonite and is responsible for the higher conductivity associated with these oxides.

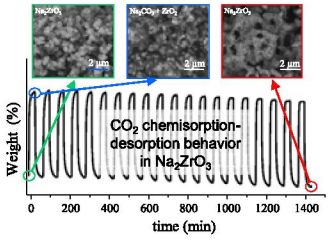

A CO_2 chemisorption–desorption analysis was performed in the Na_2ZrO_3–CO_2 system. Different cyclic experiments were performed between 500 and 800 °C and the results showed high CO_2 chemisorption efficiencies. Nevertheless the Na_2ZrO_3 composition and microstructure evolved during the cycles.

The single-crystalline hierarchical $Cu_2Cl(OH)_3$ spheres can be prepared for the first time by using a template-free process through freeze-drying. Meanwhile, the hierarchical spheres exhibited high adsorption capacity to methylene blue.

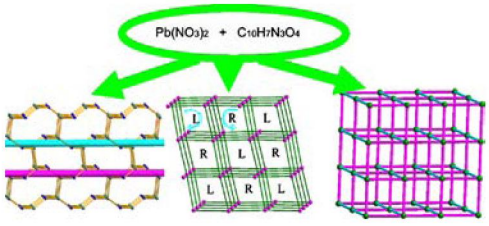

Three 3D lead compounds based on 2-(pyridin-2-yl)-1*H*-imidazole-4,5-dicarboxylic acid have been hydrothermally synthesized. Four new coordination modes of the organic ligand are first reported.

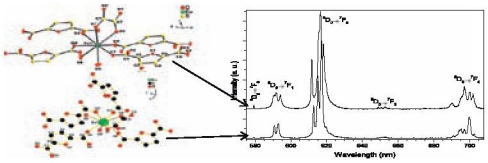

Exploring metal organic framework polymorphism in the system $Eu(H_2O)_2(fdc)(ox)_{0.5}\cdot(H_2O)]_n$ (fdc^{2-} = 2,5-furandicarboxylate, ox^{2-} = oxalate) for tuning light emission.

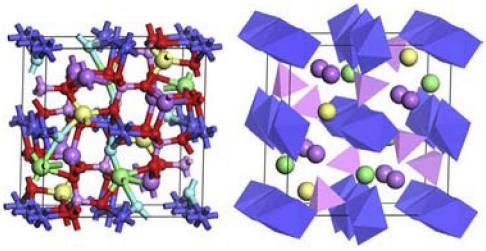

Lithium transition metal fluorophosphates (Li_2CoPO_4F and Li_2NiPO_4F).

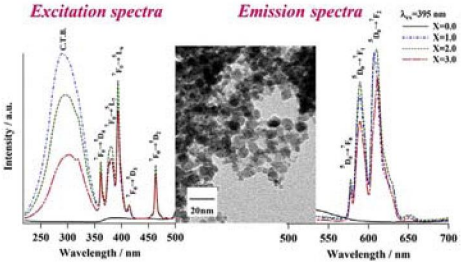

This graphical abstract shows the excitation and emission spectra and a transmission electron microscopy image of nanocrystals (with composition based on the rare-earth niobates (Ln_3NbO_7, Ln = Y, Eu) and zirconia (ZrO_2) that were composed of 50 mol% Ln_3NbO_7 and 50 mol% ZrO_2) formed via hydrothermal route.

Continued

MWCNT/WO_3 nanocomposite photoanode for visible light induced water splitting
Samira Yousefzadeh, Ali Reyhani, Naimeh Naseri and Alireza Z. Moshfegh
page 341

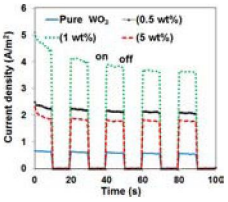

Photocurrent density versus time at constant potential (0.7 V) for the WO_3 films containing different MWCNT weight percentages annealed at 400 °C under 1000 Wm^{-2} visible photo-illumination.

Bismuth(III) dialkyldithiophosphates: Facile single source precursors for the preparation of bismuth sulfide nanorods and bismuth phosphate thin films
Jasmine B. Biswal, Shivram S. Garje, Jitendra Nuwad and C.G.S. Pillai
page 348

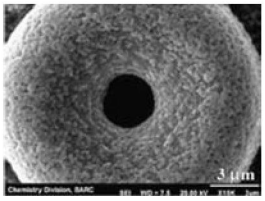

Solvothermal decomposition of bismuth(III) dialkyldithiophosphates in ethylene glycol gave Bi_2S_3 nanoparticles, whereas aerosol assisted chemical vapor deposition of these single source precursors deposited $Bi_2P_4O_{13}$ thin films.

Morphology control of open-framework zinc phosphate $Zn_4(H_3O)(NH_4)_3(PO_4)_4$ via microwave-assisted technique
Ling Ding, Yu Song, Wei Yang, Run-Miao Xue, Shang-Ru Zhai and Qing-Da An
page 356

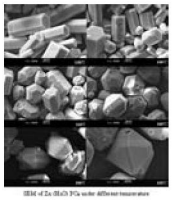

Zinc phosphates with variable morphologies can be obtained by simply tuning the microwave-heating temperatures.

Synthesis and reversible hydration behavior of the thiosulfate intercalated layered double hydroxide of Zn and Al
S. Radha, Wolfgang Milius, Josef Breu and P. Vishnu Kamath
page 362

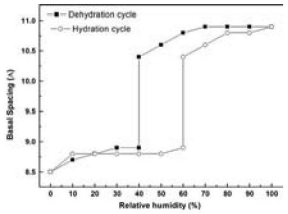

Basal spacing evolution of the thiosulfate ion intercalated [Zn–Al] LDH during one complete hydration–dehydration cycle as a function of relative humidity.

Study of $Mg_xCd_{1-x}O$ applying density functional theory: Stability, structural phase transition and electronic properties
K.B. Joshi, U. Paliwal, K.L. Galav, D.K. Trivedi and T. Bredow
page 367

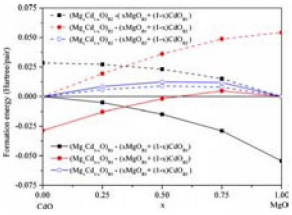

Diagram reveals trends in formation energy while mixing B2-MgO with B1-CdO to form B1-$Mg_xCd_{1-x}O$. Formation energies obtained from mixing isostructural and nonisostructural components are also shown.

Influence of surface and finite size effects on the structural and magnetic properties of nanocrystalline lanthanum strontium perovskite manganites
Pavel Žvátora, Miroslav Veverka, Pavel Veverka, Karel Knížek, Karel Závěta, Emil Pollert, Vladimír Král, Graziella Goglio, Etienne Duguet and Ondřej Kaman
page 373

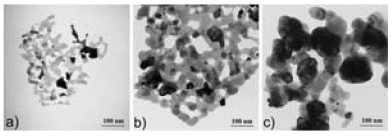

Evolution of the particle size with annealing temperature in the nanocrystalline $La_{0.70}Sr_{0.30}MnO_{3+\delta}$ phase.